OPEN ACCESS



Millimeter Observations of the Type II SN 2023ixf: Constraints on the Proximate Circumstellar Medium

Edo Berger D, Garrett K. Keating D, Raffaella Margutti D, Keiichi Maeda D, Kate D. Alexander D, Yvette Cendes D, Tarraneh Eftekhari Mark Gurwell D, Daichi Hiramatsu D, Anna Y. Q. Ho D, Tanmoy Laskar D, Tanmoy L

Department of Astronomy, Cornell University, Ithaca, NY 14853, USA
 Department of Physics & Astronomy, University of Utah, Salt Lake City, UT 84112, USA
 Department of Astrophysics/IMAPP, Radboud University, P.O. Box 9010, 6500 GL, Nijmegen, The Netherlands Received 2023 June 15; revised 2023 June 22; accepted 2023 June 22; published 2023 July 10

Abstract

We present 1.3 mm (230 GHz) observations of the recent and nearby Type II supernova, SN 2023ixf, obtained with the Submillimeter Array (SMA) at 2.6–18.6 days after explosion. The observations were obtained as part the SMA Large Program, POETS (Pursuit of Extragalactic Transients with the SMA). We do not detect any emission at the location of SN 2023ixf, with the deepest limits of $L_{\nu}(230~{\rm GHz}) \lesssim 8.6 \times 10^{25}~{\rm erg~s^{-1}~Hz^{-1}}$ at 2.7 and 7.7 days, and $L_{\nu}(230~{\rm GHz}) \lesssim 3.4 \times 10^{25}~{\rm erg~s^{-1}~Hz^{-1}}$ at 18.6 days. These limits are about a factor of 2 times dimmer than the millimeter emission from SN 2011dh (IIb), about 1 order of magnitude dimmer compared to SN 1993J (IIb) and SN 2018ivc (IIL), and about 30 times dimmer than the most luminous nonrelativistic SNe in the millimeter band (Type IIb/Ib/Ic). Using these limits in the context of analytical models that include synchrotron self-absorption and free–free absorption, we place constraints on the proximate circumstellar medium around the progenitor star, to a scale of $\sim 2 \times 10^{15}~{\rm cm}$, excluding the range $\dot{M} \sim {\rm few} \times 10^{-6} - 10^{-2}~M_{\odot}~{\rm yr^{-1}}$ (for a wind velocity, $v_w = 115~{\rm km~s^{-1}}$, and ejecta velocity, $v_{\rm ej} \sim (1-2) \times 10^4~{\rm km~s^{-1}}$). These results are consistent with an inference of the mass-loss rate based on optical spectroscopy ($\sim 2 \times 10^{-2}~M_{\odot}~{\rm yr^{-1}}$ for $v_w = 115~{\rm km~s^{-1}}$), but are in tension with the inference from hard X-rays ($\sim 7 \times 10^{-4}~M_{\odot}~{\rm yr^{-1}}$ for $v_w = 115~{\rm km~s^{-1}}$). This tension may be alleviated by a nonhomogeneous and confined CSM, consistent with results from high-resolution optical spectroscopy.

Unified Astronomy Thesaurus concepts: Supernovae (1668); Type II supernovae (1731); Core-collapse supernovae (304); Massive stars (732); Stellar mass loss (1613); Circumstellar matter (241)

1. Introduction

Over the past few decades observations of core-collapse supernovae (CCSNe) ranging from radio to X-rays have revealed that massive stars may undergo enhanced or eruptive mass loss in the final years and decades prior to core collapse (e.g., Smith 2014). The resulting circumstellar medium (CSM) around the progenitor stars can be probed using optical spectroscopy shortly after explosion, which can reveal emission from the ionized CSM (so-called flash spectroscopy; e.g., Gal-Yam et al. 2014; Yaron et al. 2017); optical/UV observations of the rising light curves, which can reveal energy deposition from CSM–supernova (SN) ejecta shock interaction (e.g., Nakar & Piro 2014; Moriya et al. 2018; Hiramatsu et al. 2021); X-ray observations, which track thermal bremsstrahlung emission from CSM–SN ejecta shock interaction and absorption by neutral CSM; and radio/millimeter observations that

Original content from this work may be used under the terms of the Creative Commons Attribution 4.0 licence. Any further distribution of this work must maintain attribution to the author(s) and the title of the work, journal citation and DOI.

trace synchrotron emission due to the acceleration of relativistic electrons in CSM–SN shock interaction (e.g., Chevalier & Fransson 2017).

SN 2023ixf was discovered on 2023 May 19.727 UT shortly after explosion in M101 (Itagaki 2023), at $d \approx 6.9$ Mpc (Riess et al. 2022), and was classified as a Type II SN shortly thereafter (Perley et al. 2023). Thanks to its early discovery and proximity, extensive data across the electromagnetic spectrum is being collected, including early optical spectra that reveal flash ionization features (Jacobson-Galan et al. 2023; Smith et al. 2023) and narrow absorption due to the preshocked CSM (Smith et al. 2023); optical light curves, which point to early excess emission (Hosseinzadeh et al. 2023); and hard X-ray observations, indicating a large neutral hydrogen column density in the vicinity of the SN (Grefenstette et al. 2023). Preexplosion Hubble Space Telescope, Spitzer Space Telescope, and ground-based observations point to a variable and dusty red supergiant progenitor (Kilpatrick et al. 2023; Neustadt et al. 2023; Pledger & Shara 2023). Here, we report on early observations obtained with the Submillimeter Array (SMA) spanning about 2.7–18.6 days after the estimated time of first light, and use these data to constrain the CSM density around the progenitor star. We present the data in Section 2 and

¹⁰ NASA Einstein Fellow.

Table 1
SMA Observations of SN 2023ixf

UT Date	δt (days)	$F_{ u}^{a}$ (mJy)	$\frac{L_{\nu}^{\text{ a}}}{(10^{26} \text{ erg s}^{-1} \text{ Hz}^{-1})}$
May 21.17–21.63	2.66	<1.5	< 0.86
May 22.17-22.29	3.49	< 3.3	< 1.89
May 24.51-24.62	5.83	< 4.2	< 2.40
May 26.34-26.62	7.74	< 1.5	< 0.86
May 28.44-28.62	9.79	< 2.4	<1.37
Jun 6.09-6.60	18.60	< 0.6	< 0.34

Note. Phases (δt) are given relative to an estimated time of first light of 2023 May 18.74 UT and are at the midpoint of each observation.

compare to previous millimeter-band data for CCSNe in Section 3 and to numerical and analytical models in Section 4. We discuss and summarize the results in Section 5.

2. Observation and Data Analysis

Following the discovery and classification of SN 2023ixf, we used the SMA on several occasions to observe the SN, starting on 2023 May 21.17, about 2.4 days after the estimated time of first light (2023 May 18.74 UT; e.g., Hosseinzadeh et al. 2023; D. Hiramatsu et al. 2023, in preparation) The observations were obtained as part of the new Large Project POETS (Pursuit of Extragalactic Transients with the SMA; project 2022B-S046, PI: Berger). The observations are summarized in Table 1. During these observations, the SMA was tuned to an local oscillator (LO) frequency of 225.5 GHz, providing spectral coverage between 209.5–221.5 and 229.5–241.5 GHz. Across all nights, 3C454.3 was observed as a bandpass calibrator, Ceres was observed as a flux calibrator, and J1419+543 and J1506+426 were observed as gain calibrators, with a 15 minute cycle time cadence.

Analysis of the data was performed using the SMA COMPASS pipeline (G. K. Keating et al. 2023, in preparation), which flags spectral data based on outliers in amplitude when coherently averaging over increasing time intervals for each channel within each baseline, as well as baselines where little-to-no coherence is seen on calibrator targets. Flux calibration was performed using the Butler–JPL–Horizons 2012 (Butler 2012) model for Ceres. The data were imaged, and deconvolution was performed via the CLEAN algorithm (Högbom 1974).

We do not detect emission from the location of SN 2023ixf in any of our observations, with rms noise levels spanning about 0.2-1.4 mJy. The corresponding luminosity limits are $\lesssim 3.4 \times 10^{25} - 2.4 \times 10^{26}$ erg s⁻¹ Hz⁻¹ (Table 1). An SMA continuum and CO(2–1) line map are shown in Figure 1 overlaid on a Hubble Space Telescope image of the field.

3. Comparison to Other Core-collapse Supernovae

In Figure 2 we show the SMA spectral luminosity upper limits for SN 2023ixf in comparison to the millimeter-band (\approx 100–250 GHz) light curves of several nearby CCSNe (Type II and Ib/c) on timescales of \sim 3–23 days. Previously detected SNe span luminosities from only a factor of about 2 times higher than our limits (e.g., SN 2011dh; Horesh et al. 2013b) and up to \sim 3 × 10²⁷ erg s⁻¹ Hz⁻¹, more than 1 order of magnitude more luminous than our limits for SN 2023ixf (e.g.,



Figure 1. Map from the aggregate SMA data from all six epochs of observations, of the region around SN 2023ixf (white cross) overlaid on a false-color Hubble Space Telescope image, with the synthesized beam shown in the lower left (white ellipse). We show contours of the 230 GHz (1.3 mm) continuum emission in red, and the CO(2–1) line emission in cyan. Continuum contours correspond to 0.6, 0.9, 1.2, and 1.5 mJy; CO(2–1) contours correspond to 2, 4, and 8 Jy km s⁻¹ (uncorrected for primary beam effects). No continuum emission is detected at the position of SN 2023ixf, which is located near NGC 5461, an H II region at the southeastern edge of M101 (white box in inset).

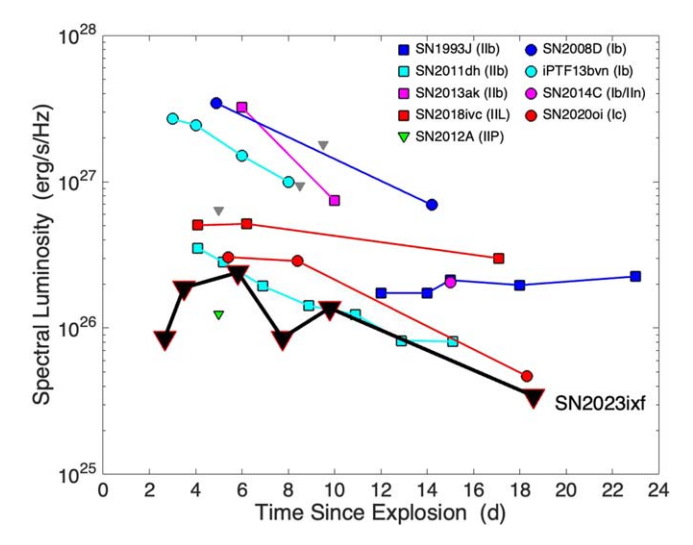


Figure 2. SMA 230 GHz upper limits for SN 2023ixf (black triangles; 3σ) compared to the existing sample of CCSNe with early millimeter-band detections (squares: Type II; circles: Type Ib/c; Weiler et al. 2007; Soderberg et al. 2008; Gorosabel et al. 2010; Chakraborti et al. 2013; Horesh et al. 2013a, 2013b; Zauderer et al. 2013b, 2014; Maeda et al. 2021), or upper limits (triangles; Carpenter 2010; Horesh et al. 2012b, 2012a; Zauderer et al. 2013a); we particularly highlight the nondetection of the Type IIP SN 2012A.

SN 2018ivc; Maeda et al. 2023). We identify only a single nondetection (Type IIP SN 2012A; Horesh et al. 2012b) that is deeper than our limits for SN 2023ixf, by about a factor of 2. In recent work Maeda et al. (2023) inferred mass-loss rates (scaled to a wind velocity of 100 km s $^{-1}$) of $\sim 10^{-3}~M_{\odot}~\rm yr^{-1}$ for SN 2018ivc, $\sim 10^{-4}~M_{\odot}~\rm yr^{-1}$ for SN 1993J, and $\sim 10^{-5}~M_{\odot}$

^a Limits are 3 times the image rms.

yr $^{-1}$ for SN 2011dh based on millimeter-band data. Comparable mass-loss rates, \sim few \times 10^{-6} – 10^{-4} M_{\odot} yr $^{-1}$, have been inferred for other Type IIb SNe based on centimeter-band data (e.g., Nayana et al. 2022 and references therein). We note that all these comparison SNe are of Type IIb or IIL with more stripped and compact progenitors than that of SN 2023ixf (Kilpatrick et al. 2023; Neustadt et al. 2023) and likely have higher velocity ejecta that boost their millimeter-band (and radio) synchrotron emission.

4. CSM Interaction Models

We use the nondetections at 230 GHz to place constraints on the CSM around the progenitor of SN 2023ixf on a scale of $\sim 2 \times 10^{14} - 2 \times 10^{15}$ cm (for an assumed ejecta velocity of $\sim 10^4$ km s⁻¹). In the millimeter band the expected emission is due to synchrotron radiation arising from shock interaction of the SN ejecta with the CSM. We consider the effects of both synchrotron self-absorption and free–free absorption by an external CSM, following the well-established models of Weiler et al. (1986) and Chevalier (1998), which have been used to interpret the radio/millimeter emission from previous CCSNe.

In the high-density limit, free–free absorption is expected to dominate, with the optical depth given by Weiler et al. (1986): $\tau_{\rm ff} = K_2 (\nu/5~{\rm GHz})^{-2.1} t_d^{-3}$, where t_d is time in days since explosion, and we have assumed that the ejecta are roughly in free expansion (leading to the temporal power-law index of -3). Setting $\tau_{\rm ff}(230~{\rm GHz}) \gtrsim 1$ at 2.7 and 18.6 days, we find $K_2 \gtrsim 6.1 \times 10^4$ and $\gtrsim 2 \times 10^7$, respectively. The mass-loss rate is given by Weiler et al. (1986):

$$\dot{M} \approx 10^{-8} \, M_{\odot} \,\mathrm{yr}^{-1} \, \tau_{\rm ff, 5~GHz}^{0.5} \, t_d^{1.5} \, (v_{\rm ej} / 10^4 \,\mathrm{km~s}^{-1})^{1.5} \\ \times \, (T_e / 10^4 \,\mathrm{K})^{0.68} \, (v_w / 10 \,\mathrm{km~s}^{-1}), \tag{1}$$

where T_e is the electron temperature, and v_w is the CSM wind velocity. Using our SMA limits at 2.7 and 18.6 days, with $v_w = 115 \text{ km s}^{-1}$ (Smith et al. 2023), $v_{\rm ej} = 10^4 \text{ km s}^{-1}$, and $T_e = 10^4 \text{ K}$, we find $\dot{M} \gtrsim 10^{-4}$ and $\gtrsim 4 \times 10^{-2} M_{\odot} \text{ yr}^{-1}$, respectively.

In the case of synchrotron self-absorption only, the inferred mass-loss rate is much lower, and is given by Chevalier (1998):

$$\dot{M} \approx 8.2 \times 10^{-7} M_{\odot} \text{yr}^{-1} \epsilon_{B,-1}^{-1} (\epsilon_e/\epsilon_B)^{-8/19} L_{26}^{-4/19} \times \nu_{230 \text{ GHz}}^2 t_d^2 (\nu_w/10 \text{ km s}^{-1}),$$
(2)

where ϵ_e and ϵ_B are the postshock energy fractions in the relativistic electrons and magnetic fields, respectively. Using our limits at 2.7 and 18.6 days, and assuming $\epsilon_e = \epsilon_B = 0.1$, we find $\dot{M} \lesssim 7 \times 10^{-5}$ and $\lesssim 4 \times 10^{-3}~M_{\odot}~{\rm yr}^{-1}$, respectively. A full analytical calculation of the effects of free–free

A full analytical calculation of the effects of free–free absorption and synchrotron self-absorption (following Chevalier 1998) is shown in Figure 3, where we constrain the joint phase space of \dot{M} and $v_{\rm ej}$ ruled out by our SMA data. In this calculation we determine the millimeter-band luminosity for a range of ejecta velocities and mass-loss rates, using an input kinetic energy, $v_w = 115$ km s⁻¹, and assuming two sets of equipartition values ($\epsilon_e = \epsilon_B = 0.1$ and $\epsilon_e = 0.1$, $\epsilon_B = 0.01$) and

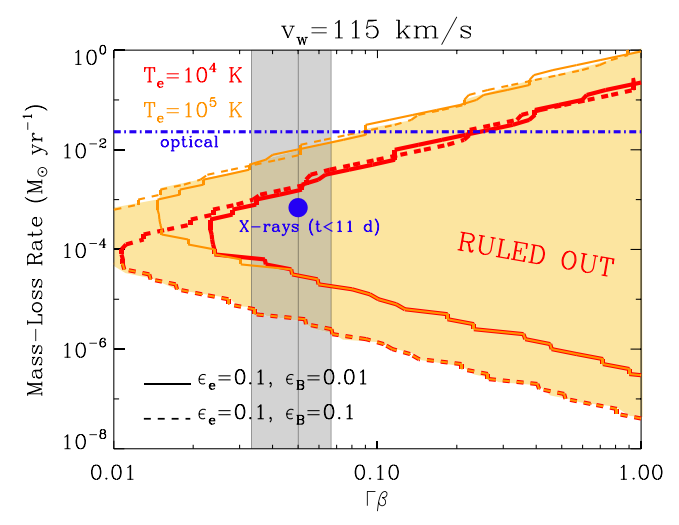


Figure 3. The phase space of progenitor mass-loss rate vs. ejecta velocity that is *excluded* by our most constraining SMA limits at 2.7, 7.7, and 18.6 days. The models (Chevalier 1998) assume $v_w = 115 \text{ km s}^{-1}$ (Smith et al. 2023) and are shown for two sets of equipartition parameters (ϵ_e and ϵ_B), an electron power-law distribution with $N_e(\gamma_e) \propto \gamma_e^{-p}$ with p=3, a volume filling factor of 0.5, and two values for the electron temperature (T_e). The vertical gray shaded region indicates an ejecta velocity range of $v_{\rm ej} = (1-2) \times 10^4 \text{ km s}^{-1}$. The blue dot marks the value of \dot{M} inferred from X-ray observations acquired at $\lesssim 11$ days (Grefenstette et al. 2023), while the horizontal blue dotted–dashed line marks the value of \dot{M} inferred from optical spectra at $\lesssim 14$ days (Jacobson-Galan et al. 2023). Both values have been updated to $v_w = 115 \text{ km s}^{-1}$.

two values for T_e (10⁴ and 10⁵ K). We find that for a reasonable range of $v_{\rm ej} = (1-2)\times 10^4$ km s⁻¹ we can *exclude* a mass-loss rate range of $\dot{M}\sim {\rm few}\times 10^{-6}-10^{-2}~M_{\odot}~{\rm yr}^{-1}$ (for $\epsilon_e=\epsilon_B=0.1$ and $T_e=10^5$ K).

The constraints shown in Figure 3 are demonstrated by a comparison between model light curves and the observed upper limits in Figure 4. Here, we use the model prescriptions described in Maeda et al. (2021) and Maeda et al. (2023). We adopt a CSM with a wind profile truncated at 2×10^{15} cm to represent a "confined" CSM. The ejecta mass and energy are set to be $11 M_{\odot}$ and 10^{51} erg, and free–free absorption is included assuming $T_{\rm e}=10^5$ K. Inverse Compton cooling is taken into account, using the r/R-band light curve (Jacobson-Galan et al. 2023) as a proxy for the bolometric light curve of SN 2023ixf. While the model here adopts the self-similar solution for the shock-wave dynamics (Chevalier 1998), it reproduces the results of the more detailed calculation by Matsuoka et al. (2019).

Adopting our fiducial values of $\epsilon_{\rm e} = \epsilon_{\rm B} = 0.1$, we find that the 230 GHz upper limits for SN 2023ixf rule out $\dot{M} \sim 5 \times 10^{-6} - 2 \times 10^{-3}~M_{\odot}~{\rm yr}^{-1}$, comparable to the model exclusion region shown in Figure 3. A key point is that the model accounts for the deceleration of the outer ejecta, which is important in the case of the high mass-loss rate regime (this means that we need to evaluate the constraints on mass-loss rate at somewhat different velocities for the lower and upper bounds in Figure 3). Additionally, we stress that the choice of (unconstrained) microphysical parameters ($\epsilon_{\rm e}$ and $\epsilon_{\rm B}$) are important, as demonstrated in the right panel of Figure 4 where we adopt the smaller values inferred for SN 2020oi (Maeda et al. 2021). In this case, the allowed range of the massloss rate is $\dot{M} \lesssim 5 \times 10^{-5}~M_{\odot}~{\rm yr}^{-1}$ or $\gtrsim 2 \times 10^{-3} M_{\odot}~{\rm yr}^{-1}$; interestingly, an intermediate mass-loss rate of $\sim 10^{-4}~M_{\odot}~{\rm yr}^{-1}$ is marginally allowed. In any case, it is important to use additional information such as the inverse Compton cooling or

 $[\]overline{^{11}}$ As noted by Lundqvist & Fransson (1988), time-dependent heating and recombination in the CSM may impact the inferred value of \dot{M}/ν_w , compared to a fiducial assumption of a fully ionized, 10^4 K CSM, primarily due to higher temperatures in the CSM. However, this results in only a factor of \sim 2–3 difference, and here we also consider a higher temperature of 10^5 K that should provide a reasonable range.

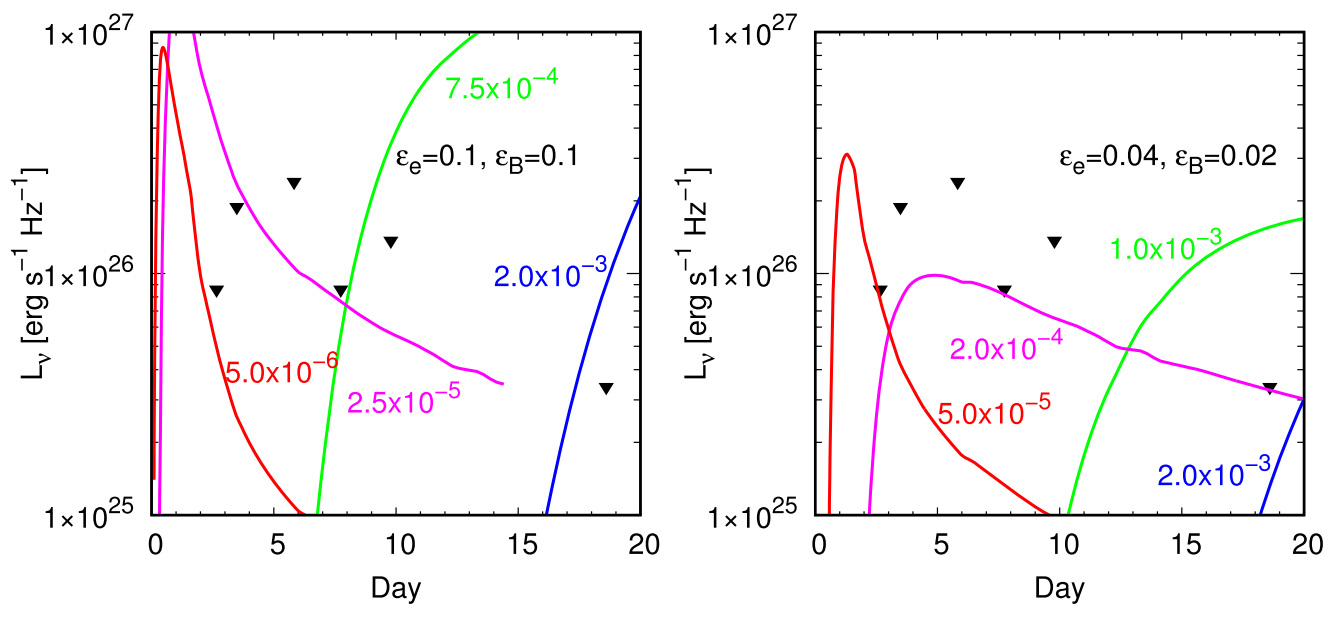


Figure 4. Model light curves at 230 GHz (lines) using the formalism of Maeda et al. (2021) and Maeda et al. (2023) for several choices of the mass-loss rate and for two sets of equipartition parameters: $\epsilon_e = \epsilon_B = 0.1$ (left) and $\epsilon_e = 0.04$ and $\epsilon_B = 0.02$ (right; calibrated with models for SN 2020oi: Maeda et al. 2023). The triangles are the upper limits for SN 2023ixf.

multiwavelength information to robustly constrain the massloss rate (e.g., Maeda et al. 2023).

In recent work, Jacobson-Galan et al. (2023) estimated a mass-loss rate of $\dot{M} \sim 10^{-2} \, M_{\odot} \, {\rm yr}^{-1}$ to a scale of $\sim 10^{15} \, {\rm cm}$ by comparing the ionization features in early optical spectra (extending to about 14 days) with spectral models of CSM interaction. This result is marked in Figure 3 and is in agreement with the results presented here. On the other hand, Grefenstette et al. (2023) used hard X-ray data at 4 and 11 days to estimate $\dot{M} \sim 3 \times 10^{-4} \ M_{\odot} \ \rm yr^{-1}$ on a similar radial scale (or $\sim 7 \times 10^{-4} \ M_{\odot} \ \rm yr^{-1}$ if using $v_w = 115 \ \rm km \ s^{-1}$; see Figure 3). This value is in tension with our results for $T_e = 10^5$ K and marginally for $T_e = 10^4$ K. However, it is essential to note that each of these approaches to determining the CSM density makes key simplifying assumptions that may lead to disparate estimates of the CSM properties. This includes numerical factors (e.g., ϵ_e , ϵ_B , and T_e in our case) and underlying geometrical assumptions such as spherical symmetry and a homogeneous CSM. For example, it is possible that a nonhomogeneous and radially confined CSM, which may also affect the ejecta velocity angular profile, would lead to X-ray and millimeter emission regions of different densities. Indeed, an asymmetric and confined CSM on a radial scale of $\sim 10^{15}$ cm has been inferred from high-resolution optical spectroscopy (Smith et al. 2023).

5. Conclusions

We have presented millimeter-band observations of the recently discovered SN 2023ixf, covering about 2.7–18.6 days after explosion. The nondetections place an upper bound on the luminosity at 230 GHz of \lesssim 8.6 \times 10²⁵ erg s⁻¹ Hz⁻¹ at 2.7 and 7.7 days, and \lesssim 3.4 \times 10²⁵ erg s⁻¹ Hz⁻¹ at 18.6 days. These limits are about a factor of 2 times lower than the millimeterband emission detected from SN 2011dh (IIb) and about 1 order of magnitude lower than the emission in SN 1993J (IIb) and SN 2018ivc (IIL). Using these limits, we place constraints on the proximate CSM of the progenitor of SN 2023ixf, out to a

scale of \sim few \times 10¹⁵ cm of $\dot{M} \gtrsim 10^{-2}~M_{\odot}~\rm{yr}^{-1}$ (free–free absorption) or $\lesssim 10^{-6}~M_{\odot}~\rm{yr}^{-1}$ (synchrotron self-absorption). We note that these limits are in agreement with the inferences from early optical spectroscopy (Jacobson-Galan et al. 2023; Smith et al. 2023) but are in tension with the inferred mass loss based on early X-ray observations (Grefenstette et al. 2023). A likely scenario that may alleviate this tension is a nonhomogeneous and confined dense CSM (Smith et al. 2023), which can lead to the X-ray emission emerging from lower density regions while the millimeter-band emission is absorbed.

We anticipate that continued observations of SN 2023ixf in the radio/millimeter and X-ray regimes over the coming weeks, months, and years, as well as joint modeling with the available optical photometry and spectroscopy, will eventually better delineate the complex and likely nonspherical and nonhomogeneous CSM environment of the progenitor. More broadly, as demonstrated here, early millimeter-band observations can provide constraints on the density and geometry of the CSM around SN progenitors on the same spatial scales as rapid optical spectroscopy and X-ray observations, providing an independent constraint with different modeling assumptions. We plan to continue undertaking such observations for nearby CCSNe as part of POETS.

Acknowledgments

The Berger Time-Domain research group at Harvard is supported by the NSF and NASA. T.E. is supported by NASA through the NASA Hubble Fellowship grant HST-HF2-51504.001-A awarded by the Space Telescope Science Institute, which is operated by the Association of Universities for Research in Astronomy, Inc., for NASA, under contract NAS5-26555. K.M. acknowledges support from JSPS KAKENHI grant JP20H00174.

The Submillimeter Array is a joint project between the Smithsonian Astrophysical Observatory and the Academia Sinica Institute of Astronomy and Astrophysics and is funded by the Smithsonian Institution and the Academia Sinica. We

recognize and acknowledge that Maunakea is a culturally important site for the indigenous Hawaiian people, and we are privileged to study the cosmos from its summit.

Facility: SMA

ORCID iDs

Edo Berger https://orcid.org/0000-0002-9392-9681
Garrett K. Keating https://orcid.org/0000-0002-3490-146X
Raffaella Margutti https://orcid.org/0000-0003-4768-7586
Keiichi Maeda https://orcid.org/0000-0003-2611-7269
Kate D. Alexander https://orcid.org/0000-0002-8297-2473
Yvette Cendes https://orcid.org/0000-0001-7007-6295
Tarraneh Eftekhari https://orcid.org/0000-0003-0307-9984
Mark Gurwell https://orcid.org/0000-0003-0307-9984
Mark Gurwell https://orcid.org/0000-0003-0685-3621
Daichi Hiramatsu https://orcid.org/0000-0002-1125-9187
Anna Y. Q. Ho https://orcid.org/0000-0002-9017-3567
Tanmoy Laskar https://orcid.org/0000-0003-1792-2338
Ramprasad Rao https://orcid.org/0000-0002-1407-7944
Peter K. G. Williams https://orcid.org/0000-0003-3734-3587

References

```
Butler, B. 2012, Atacama Large Millimeter/Submillimeter Array Memo 594 Carpenter, J. M. 2010, ATel, 2863, 1 Chakraborti, S., Petitpas, G., Zauderer, A., et al. 2013, ATel, 4947, 1 Chevalier, R. A. 1998, ApJ, 499, 810 Chevalier, R. A., & Fransson, C. 2017, in Handbook of Supernovae, ed. A. W. Alsabti & P. Murdin (Berlin: Springer), 875 Gal-Yam, A., Arcavi, I., Ofek, E. O., et al. 2014, Natur, 509, 471 Gorosabel, J., de Ugarte Postigo, A., Castro-Tirado, A. J., et al. 2010, A&A, 522, A14 Grefenstette, B. W., Brightman, M., Earnshaw, H. P., Harrison, F. A., &
```

Margutti, R. 2023, arXiv.2306.04827

```
Hiramatsu, D., Howell, D. A., Van Dyk, S. D., et al. 2021, NatAs, 5, 903
Högbom, J. A. 1974, A&AS, 15, 417
Horesh, A., Cao, Y., Mooley, K., & Carpenter, J. 2013a, ATel, 5198, 1
Horesh, A., Carpenter, J., & Kulkarni, S. R. 2012a, ATel, 3885, 1
Horesh, A., Carpenter, J., Kulkarni, S. R., & Kasliwal, M. 2012b, ATel,
Horesh, A., Stockdale, C., Fox, D. B., et al. 2013b, MNRAS, 436, 1258
Hosseinzadeh, G., Farah, J., Shrestha, M., et al. 2023, arXiv:2306.06097
Itagaki, K. 2023, TNSTR, 1158, 1
Jacobson-Galan, W. V., Dessart, L., Margutti, R., et al. 2023, arXiv:2306.
Kilpatrick, C. D., Foley, R. J., Jacobson-Galán, W. V., et al. 2023, arXiv:2306.
  04722
Lundqvist, P., & Fransson, C. 1988, A&A, 192, 221
Maeda, K., Chandra, P., Matsuoka, T., et al. 2021, ApJ, 918, 34
Maeda, K., Chandra, P., Moriya, T. J., et al. 2023, ApJ, 942, 17
Matsuoka, T., Maeda, K., Lee, S.-H., & Yasuda, H. 2019, ApJ, 885, 41
Moriya, T. J., Förster, F., Yoon, S.-C., Gräfener, G., & Blinnikov, S. I. 2018,
   MNRAS, 476, 2840
Nakar, E., & Piro, A. L. 2014, ApJ, 788, 193
Nayana, A. J., Chandra, P., Krishna, A., & Anupama, G. C. 2022, ApJ,
  934, 186
Neustadt, J. M. M., Kochanek, C. S., & Rizzo Smith, M. 2023, arXiv:2306.
Perley, D. A., Gal-Yam, A., Irani, I., & Zimmerman, E. 2023, TNSAN, 119, 1
Pledger, J. L., & Shara, M. M. 2023, arXiv:2305.14447
Riess, A. G., Yuan, W., Macri, L. M., et al. 2022, ApJL, 934, L7
Smith, N. 2014, ARA&A, 52, 487
Smith, N., Pearson, J., Sand, D. J., et al. 2023, arXiv:2306.07964
Soderberg, A. M., Berger, E., Page, K. L., et al. 2008, Natur, 453, 469
Weiler, K. W., Sramek, R. A., Panagia, N., van der Hulst, J. M., & Salvati, M.
  1986, ApJ, 301, 790
Weiler, K. W., Williams, C. L., Panagia, N., et al. 2007, ApJ, 671, 1959
Yaron, O., Perley, D. A., Gal-Yam, A., et al. 2017, NatPh, 13, 510
Zauderer, A., Kamble, A., Chakraborti, S., & Soderberg, A. 2013a, ATel,
  4866, 1
Zauderer, A., Soderberg, A., Chakraborti, S., et al. 2013b, ATel, 4946, 1
Zauderer, B. A., Kamble, A., Chakraborti, S., & Soderberg, A. 2014, ATel,
  5764, 1
```